Expected improvements in determining continental hydrology, ice mass variations, ocean bottom pressure signals, and earthquakes using two pairs of dedicated satellites for temporal gravity recovery

David N. Wiese,[1] Robert S. Nerem,[1,2] and Shin-Chan Han[3]

Received 18 March 2011; revised 13 August 2011; accepted 6 September 2011; published 19 November 2011.

[1] The Gravity Recovery and Climate Experiment mission has demonstrated the ability to quantify global mass variations at large spatial scales with monthly to sub-monthly temporal resolution. Future missions of this type taking advantage of improved measurement technologies will be limited by temporal aliasing errors. We suggest the addition of a second pair of satellites to reduce these errors. Using an optimized mission architecture consisting of a polar pair of satellites coupled with a lower inclined pair of satellites (72°), both in 13-day repeating orbits, we quantify the expected scientific improvements that having two pairs of satellites will provide over one pair. Numerical simulations to spherical harmonic degree 100 are run over one full year. Analysis using empirical orthogonal functions reveals that two satellite pairs determine annual mass variations in small basins which are undetected using one pair of satellites. Averaging kernels are used to show that two satellite pairs offer an 80% reduction in the level of error in determining mass variations in 53 hydrological basins and 12 Greenland basins over the year. After standard GRACE post-processing techniques have been applied to the one-pair solutions, it is seen that two satellite pairs (with no post-processing) still offer a 25%–75% improvement in determining the mass variations. Spatiospectral localization analysis is used to show increased spatial resolution and higher signal-to-noise ratios in recovering hydrology in the Amazon River basin, ocean bottom pressure signals in the Southeast Pacific basin, and a simulated earthquake signal representative of the 2010 Maule, Chile earthquake.

Citation: Wiese, D. N., R. S. Nerem, and S.-C. Han (2011), Expected improvements in determining continental hydrology, ice mass variations, ocean bottom pressure signals, and earthquakes using two pairs of dedicated satellites for temporal gravity recovery, *J. Geophys. Res.*, *116*, B11405, doi:10.1029/2011JB008375.

1. Introduction

[2] The Gravity Recovery and Climate Experiment (GRACE) satellite mission consists of two identical satellites in polar orbits separated by 220 km at a mean orbital altitude of 480 km. GRACE infers mass variations over the globe by measuring the change in distance between the two spacecraft with a microwave ranging instrument. This remarkable data set has allowed scientists to quantify the rate that ice sheets and glaciers are melting, mass fluxes across large river basins, global ocean mass, and large earthquakes, to name a few. GRACE resolves these signals at large spatial scales (typically 160,000 km^2, corresponding to spherical harmonic degree 50, is viewed as a limit on the spatial resolution) and monthly to sub-monthly (10-day) temporal resolution [*Tapley et al.*, 2004; *Bruinsma et al.*, 2009]. GRACE is limited by instrument errors, system errors, temporal aliasing errors, and an anisotropic sensitivity due to the formation type; however, the dominant source of error is not yet fully understood.

[3] It is expected that future missions designed to measure temporal gravity variations will take advantage of improved technologies and sensors. For example, the microwave ranging instrument is expected to be replaced with a laser interferometer [*Pierce et al.*, 2008; *Bender et al.*, 2003], increasing the precision of the inter-satellite ranging measurements from the micrometer level to the nanometer level. Additionally, the spacecraft could fly drag-free at a much lower altitude, similar to the Gravity field and steady state Ocean Circulation Explorer (GOCE) mission, lowering the error associated with the measurement of non-conservative forces [*Battrick*, 1999]. Studies have shown that adopting these new technologies for future missions will likely result

[1]Colorado Center for Astrodynamics Research, Department of Aerospace Engineering Sciences, University of Colorado at Boulder, Boulder, Colorado, USA.
[2]Cooperative Institute for Research in Environmental Sciences, University of Colorado at Boulder, Boulder, Colorado, USA.
[3]Planetary Geodynamics Laboratory, NASA Goddard Space Flight Center, Greenbelt, Maryland, USA.

Copyright 2011 by the American Geophysical Union.
0148-0227/11/2011JB008375

in the error budget being dominated by temporal aliasing errors [*Visser et al.*, 2010; *Loomis*, 2009].

[4] Temporal aliasing errors fall into two categories: (1) errors due to undersampling signals of interest (such as hydrology), and (2) errors due to mismodeling unwanted high frequency mass variations (such as the atmosphere and ocean tides) [*Han et al.*, 2004; *Thompson et al.*, 2004]. Given the fact that these errors will likely dominate future missions, it is desirable to consider methods to reduce them. One practical method is to increase the sampling frequency of the mission by adding additional satellite pairs [*Visser et al.*, 2010; *Reubelt et al.*, 2009; *van Dam et al.*, 2008]. While one could theoretically reduce temporal aliasing errors to zero (disregarding the issue of signal separation) by flying dozens of satellites pairs, we are interested in the more economically feasible option of adding only one additional pair of satellites. Having two pairs of satellites not only increases the sampling frequency of the mission, reducing the level of temporal aliasing errors, but also reduces the level of striping in the solutions should one of the satellite pairs be at a lower inclination due to the addition of East-West information to the observable [*Bender et al.*, 2008].

[5] Several studies have been carried out to address the expected improvements in performance that adding additional satellite pairs would provide in recovering temporal gravity variations [*Visser et al.*, 2010; *Elsaka*, 2010; *Wiese et al.*, 2009]. Each of these studies has been limited, however, by considering only selected mission architectures for analysis; in essence, they have been point case studies. A more recent study [*Wiese et al.*, 2011a], addressed this issue, and via a Monte-Carlo analysis involving numerical simulations, gave recommendations for selecting orbital parameters to provide near-optimal results for a mission architecture consisting of two satellite pairs. While providing the foundation for selecting the proper orbits, the expected improvements in performance that an optimized two-pair architecture would offer over a single satellite pair architecture were not discussed in detail. This paper builds on the results presented by *Wiese et al.* [2011a], by selecting a near-optimal two-pair mission architecture and quantifying the expected improvements in determining hydrology, ice mass variations (particularly in Greenland), ocean bottom pressure signals, and earthquakes. Results are analyzed on both a global and regional scale.

2. Methodology

2.1. Orbit Selection

[6] The search space for selecting an optimal set of orbital parameters for two satellite pairs with the goal of recovering temporal gravity variations is infinite. In fact, speaking strictly in terms of the satellite orbits, the mission performance is a function of 15 variables: the position and velocity of the lead spacecraft of each pair, the separation distance between each pair, and the length of time that data are accumulated. After assuming that the satellites are in circular, repeating orbits, and separated by 100 km, *Wiese et al.* [2011a] used a Monte-Carlo type of analysis with numerical simulations to spherical harmonic degree and order 100 to reduce the search space to two variables with the utmost impact on mission performance: the repeat period of both satellite pairs k, (shown to be near-optimal when they are equal to each other) expressed in nodal days, and the inclination of one of the satellite pairs i_2 (the other pair is assumed to be in a polar orbit). Note that only repeating orbits were considered, so as to guarantee consistency between solutions, which is something that GRACE lacks. Although the inter-satellite separation distance was fixed at 100 km based on anticipated instrument requirements, it should be noted that this parameter does affect the quality of the gravity solutions. As such, with the previously mentioned assumptions, the mission performance, P, can be described to first order as

$$P \approx f(k, i_2). \tag{1}$$

[7] Furthermore, the selected architecture was shown to depend on the specific scientific goals of the mission as well as the targeted altitude for the mission. When selecting a nominal measurement altitude, there is a constant trade-off of gaining improved sensitivity to short wavelength features in the gravity field at lower altitudes at the expense of a shortened mission lifetime due to increased atmospheric drag forces. *Wiese et al.* [2011a] selected a minimum allowable altitude of 290 km based on a projected 10-year mission lifetime assuming drag-free control operation of the spacecraft (analysis performed by *Marchetti et al.* [2008] and *St. Rock et al.* [2006]) and the same initial mass propellant fraction as GRACE. It was found that given the scientific objectives of determining hydrology, ice mass variations, and ocean bottom pressure signals with high spatial resolution, a near-optimal architecture of this type is found when $11 \leq k \leq 14$ and $70° \leq i_2 \leq 75°$.

[8] Using the results from *Wiese et al.* [2011a], we select a near-optimal two-pair architecture consisting of a polar pair of satellites at 320 km coupled with a lower inclined pair of satellites at 72° at 290 km, both pairs being in 13-day repeating ground tracks. This architecture ensures a ground track pattern where the two pairs of satellites cross each other at constant lines of latitude. While perhaps not yet fully exploited, a ground track pattern of this type is expected to be beneficial for future missions, allowing for consistent synoptic mapping of time variable gravity variations. The architecture involving one pair of satellites chosen for comparison consists of the same polar pair of satellites that is in the two-pair architecture: a pair at 320 km in a 13-day repeating orbit. Figure 1 shows the ground tracks of the two-pair case with the polar pair being in blue and the lower inclined pair being in red. Note that the lower inclined pair geographically extends to cover the southern half of Greenland as well as the western Antarctic peninsula. The ground track from the one-pair architecture is given by the polar pair (blue) track alone. Figure 1b shows the spacing at the equator between adjacent tracks is 1.75° for the one-pair case, allowing for solutions up to degree and order 100 based on the Colombo-Nyquist rule [*Colombo*, 1984]. All analyses and comparisons made in this paper involve these selected architectures. The case of having two polar pairs of satellites is also discussed in section 3.

2.2. Numerical Simulation

[9] Numerical simulations are necessary to perform an in-depth analysis of this type. GEODYN [*Pavlis et al.*, 2010] (an orbit determination software package) and SOLVE

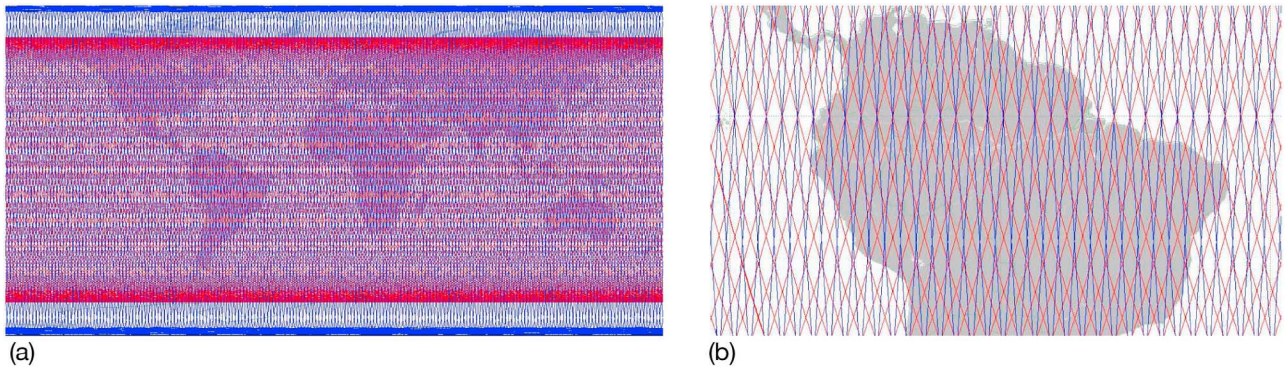

Figure 1. Ground track over 13 days for the two-pair architecture showing the polar pair (blue) and lower inclined pair (red) for (a) the entire globe and (b) over the Amazon River Basin. The ground track from the one-pair architecture is given by the blue ground track alone.

[*Ullman*, 1997] (a large linear systems solver), both provided by Goddard Space Flight Center, are used to perform the numerical simulations. The numerical simulation procedure is identical to that described by *Wiese et al.* [2011a], where the majority of the details are provided. A summary of the procedure is provided here. Table 1 shows the design of the simulation and model definitions for hydrology, atmosphere, oceans, tides, and ice mass variations. This simulation is designed to recover ice mass variations (given by the ESA model [*van Dam et al.*, 2008]) and continental hydrology (given by the GLDAS model [*Rodell et al.*, 2004]) in the presence of model errors due to the atmosphere (defined as the difference between ECMWF [*Klinker et al.*, 2000] and NCEP [*Kalnay et al.*, 1996], oceans (defined as the difference between OMCT [*Flechtner*, 2007] and MOG-2D [*Carrère and Lyard*, 2003], and tides (defined as the difference between FES2004 [*Lyard et al.*, 2006] and GOT00 [*Ray*, 1999], as well as measurement system errors. The static gravity field model is given by EIGEN-GL04C [*Förste et al.*, 2008]. Ocean bottom pressure variations are calculated by treating the NCEP and MOG-2D models as forward models, estimating corrections to them, and then examining differences with respect to the *truth* models over the oceans. All models have either 3-hour or 6-hour temporal resolution, and are interpolated linearly during the numerical simulation process. All simulations are performed for the year 2003.

[10] The satellites are assumed to be equipped with a laser interferometer which replaces the K-band microwave ranging instrument on GRACE. The measurement noise associated with the laser interferometer is taken to be 5 $nm/\sqrt{Hz}$ and is frequency independent from 10^{-3} Hz to 10^{-1} Hz, and includes an inverse correlation to frequency due to thermal effects from 10^{-5} Hz to 10^{-3} Hz [*Alnis et al.*, 2008; *Mueller et al.*, 2005; *Pierce et al.*, 2008;*Wiese et al.*, 2009]. The spacecraft are also assumed to implement a drag-free control system to counteract non-conservative forces in real time. The noise associated with this system is taken to be 0.01 $nm/s^2/\sqrt{Hz}$, which is the level that the GOCE accelerometers are capable of observing variations of the remaining non-gravitational accelerations [*Battrick*, 1999]. Errors in the position of the spacecraft are accounted for by adding white noise with a 1 cm RMS in all three directional components.

[11] The simulation process is performed in three steps. First, the spacecraft states are estimated using range-rate residuals coupled with spacecraft position measurements. Second, using the updated spacecraft state, corrections to the geopotential coefficients and the spacecraft states are made using only the updated range-rate residuals after converting the state to baseline elements according to *Rowlands et al.* [2002]. The third step involves combining daily batches of data using SOLVE into a final multiday estimate of the gravity field. Additionally, in this analysis, daily low degree and order gravity fields are estimated simultaneously in an effort to reduce temporal aliasing errors. For the case of two satellite pairs, we estimate 18 × 18 gravity fields every day, as this has been shown to be near-optimal [*Wiese et al.*, 2011b]. For the case of a single pair of satellites, high frequency/low resolution gravity fields are not estimated since the solutions necessitate the standard post-processing procedures associated with GRACE (removal of correlated errors and smoothing of the solutions), negating any reduction in errors that performing the daily (or 2-day) estimates provides. For an in-depth discussion on how and why we estimate daily low degree and order gravity fields, the reader is referred to *Wiese et al.* [2011b].

3. Results: A Global Perspective

[12] Prior to performing regional analysis, it is useful to examine the errors on a global basis to gain insights into necessary post-processing techniques. Figure 2 shows the logarithm of the formal errors (Figures 2a and 2b) along with the actual errors (Figures 2c and 2d) for a simulation designed to recover hydrology and ice mass variations, as illustrated in Table 1. The covariance analysis indicates that two pairs of satellites are expected to have substantially

Table 1. Simulation and Model Definitions

Models	Truth	Nominal
Static gravity field	EIGEN-GL04C	EIGEN-GL04C
Ocean tide model	FES2004	GOT00
Atmospheric model	ECMWF	NCEP
Ocean model	OMCT	MOG-2D
Hydrological model	GLDAS	none
Ice model	ESA	none

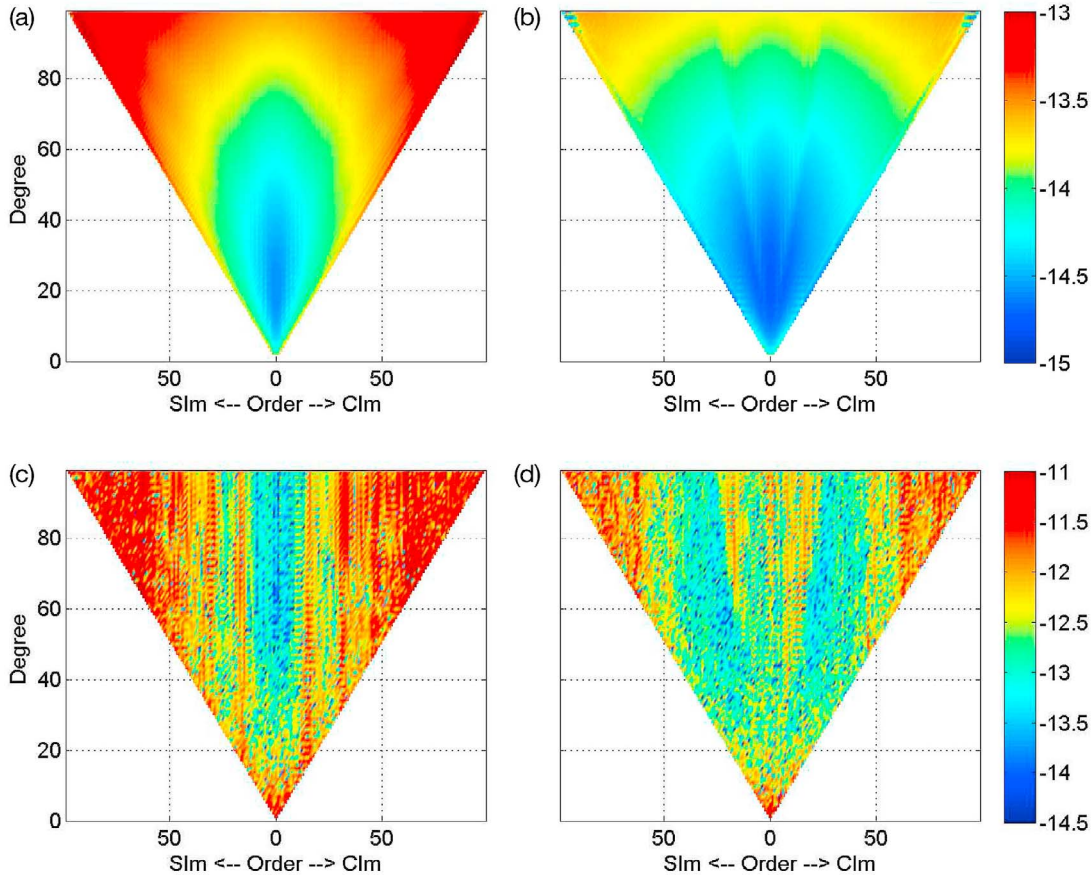

Figure 2. Logarithm of the formal error of the spherical harmonic coefficients for (a) one pair of satellites and (b) two pairs of satellites, along with the logarithm of the actual error in the spherical harmonic coefficients for (c) one pair of satellites and (d) two pairs of satellites.

lower errors for the entire spectral domain of spherical harmonic coefficients, with particular improvements in determining the sectorials and near-sectorials. For the case of a single pair of satellites, the actual errors show that higher degree and order tesseral harmonics are poorly determined, as is expected via the covariance analysis. Additionally, it is seen that the actual errors manifest themselves at the resonant order and multiples of the resonant order (m = 16, 32, 48, ..). These can be reduced via estimating empirical accelerations with a frequency of once per revolution, twice per revolution, and so on. Many of the GRACE processing centers employ this step during their estimation schemes. While we have found that this step does reduce the errors at the resonant order and multiples of the resonant order, the resulting gravity field estimate still has longitudinal stripes, requiring standard post-processing procedures, as discussed in the following paragraph. Once these post-processing procedures have been invoked, there are negligible differences in the resulting gravity field estimates whether we estimate empirical once per revolution and twice per revolution acceleration terms or not; hence, we forgo this step. With the addition of the lower inclined pair of satellites, the bands of error at the resonant order and multiples of the resonant order diminish substantially. The highest errors are seen at the high degree and order tesseral harmonic coefficients, beginning at approximately degree 60. The larger errors for high degree and low order coefficients are a localized effect over the polar regions at latitudes greater than 72° where only North-South information is present in the observable.

[13] Users of the GRACE data have developed multiple techniques for post-processing of the data tailored to optimize mass recovery of specific geophysical signals. Typically, there are two ever present problems associated with the data that must be addressed: 1) Errors at high degrees tend to dominate the gravity solutions (seen in Figure 2), and (2) correlations between coefficients of a particular order and the same parity of degree lead to longitudinal striping in the gravity solutions. Several methods have been devised to handle (1) and (2) both collectively and independently. Techniques for handling (1) independently involve spatial smoothing of the data [*Jekeli*, 1981; *Wahr et al.*, 1998; *Han et al.*, 2005; *Chen et al.*, 2006; *Guo et al.*, 2010]. These techniques can reduce the effects of (2) as well if a large enough smoothing radius is selected. Filters devised to handle (2) independently (some of which simultaneously address (1)), can be classified into two categories: empirical filters not reliant on outside information [*Swenson and Wahr*, 2006; *Chambers*, 2006; *Chen et al.*, 2007; *Schrama et al.*, 2007; *Wouters and Schrama*, 2007; *Davis et al.*, 2008; *Duan et al.*, 2009], and filters which make use of error-covariance information [*Kusche*, 2007; *Klees et al.*, 2008; *Save*, 2009]. Each of these techniques has advantages and disadvantages: some

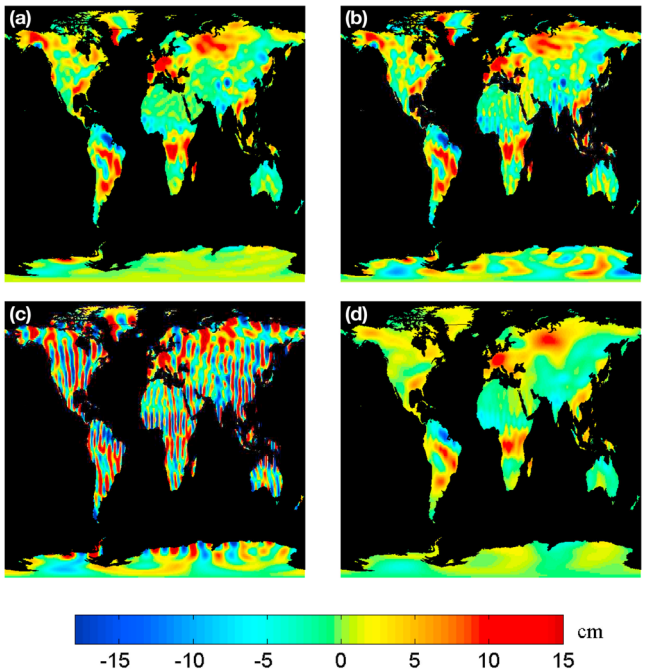

Figure 3. (a) Truth hydrology and ice signals along with the recovered hydrology and ice signals from: (b) two pairs of satellites, (c) one pair of satellites, and (d) one pair of satellites DS averaged over 13 days. Units are in cm of EWH.

reducing errors more than others, and some requiring less computation time than others. Due to lack of error-covariance information and desiring a relatively easy and computationally efficient process to account for the errors, typical users of the GRACE data tend to remove correlated errors via an empirical filter similar to *Swenson and Wahr* [2006] and reduce errors at high degrees via Gaussian smoothing [*Jekeli*, 1981]. As such, these are the two processes we employ when analyzing the solutions obtained from one pair of satellites.

[14] The solutions using two pairs of satellites have a completely different error spectrum than that of one pair, as illustrated in Figure 2. High degree and order tesseral harmonics still dominate the error budget, but the errors are much lower. Correlations between coefficients still exist, but are substantially reduced. As such, an entirely different suite of post-processing tools could be developed for analyzing solutions of this type. Rather than developing these techniques for a hypothetical mission, it is much more desirable to develop a simple, consistent method to analyze the results. Given that the errors are much lower, and do not increase substantially until approximately degree 60, it was determined that the two-pair solutions would be truncated at degree 60, and the results would be analyzed with no post-processing of the data. It was found that if the degree of truncation is increased beyond 60, the error in the high degree coefficients manifests as longitudinal stripes, requiring the development of an optimized filter to remove them. It is possible that the degree of truncation could be increased in combination with tailored filters to then gain additional spatial resolution in the solutions over those presented here.

[15] The increased spatial resolution that two pairs of satellites offers over one pair is illustrated in both the spatial domain (Figure 3) as well as the spectral domain (Figure 4). Figure 3 shows the truth hydrology and ice signals (Figure 3a), along with the recovered signal using two pairs of satellites (Figure 3b), the recovered signal using one pair of satellites (Figure 3c), and the recovered signal using one pair of satellites that has been destriped via *Swenson and Wahr* [2006] and smoothed with a 300 km Gaussian averaging radius (Figure 3d). All destriped and smoothed solutions will be denoted as 'DS' throughout the paper, and all one-pair solutions will be smoothed with a 300 km Gaussian averaging radius unless otherwise noted. The solutions are averaged over a single 13-day timespan, have been truncated at degree 60, and are expressed in cm of equivalent water height (EWH).

[16] Figure 3 illustrates that while the solutions from one pair of satellites necessitate the destriping and smoothing processes when studying signals to degree 60, as described above, the solutions using two pairs of satellites require much less. While the destriping and smoothing processes substantially reduce the level of error in the one-pair solutions, it is also seen that the geophysical signals are damped and smoothed with respect to the truth signals. The two-pair solution retains much of the spatial information that the destriping and smoothing processes remove from the one-pair solutions. It should also be mentioned that the case of having two polar pairs of satellites has been studied in conjunction with the two cases presented here. Results from this architecture are not presented in this article, however. It was found that while an architecture consisting of two polar pairs does have slightly lower errors than the case of a single polar pair, this architecture has a similar error pattern as that of one satellite pair, and correlations between coefficients of a fixed order and same parity of degree are still strong. These correlations result in longitudinal striping dominating the solution, which is also the case for one pair of satellites, as seen in Figure 3c. As such, the solutions necessitate the standard destriping and smoothing processes, and the resulting post-processed gravity field models are nearly identical to those produced using one pair of satellites (with the same post-processing). It can then be assumed that minimal increases in spatial resolution (although the temporal resolution will be increased by a factor of two) will be seen by simply adding a second polar pair of satellites.

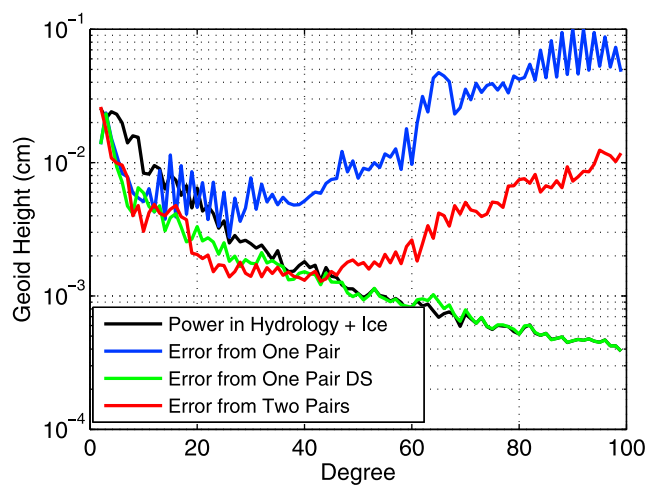

Figure 4. Geoid degree error for architectures consisting of one and two pairs of satellites.

[17] Figure 4 shows the error in terms of geoid height in determining hydrology and ice mass variations over a particular 13-day timespan as a function of spherical harmonic degree of the gravity field l for both cases. Generally, the expected spatial resolution is approximated by ~40,000/2l km. It is seen that with one pair of satellites, the errors become larger than the signal that is being estimated somewhere between degree 15 and 25 (corresponding to basin sizes of 800 and 1300 km), while using two satellite pairs increases the spatial resolution to approximately 450 km (corresponding to degree 45). Figure 4 indicates that after the solutions from one pair of satellites are destriped and smoothed, the spatial resolution increases to be approximately commensurate with that of two satellite pairs. One cannot, however, take the results in Figure 4, and assume that one pair of satellites after post-processing provides the same spatial resolution that two pairs of satellites provides (a visual inspection of Figure 3 reveals the inaccuracies with such an assumption). A global analysis of this kind is insufficient, as it disregards the different spatial distributions of signals and errors, as pointed out by *Han and Ditmar* [2008]. As such, regional analyses are necessary to more accurately quantify the expected improvements that the addition of a second pair of satellites provides.

[18] Finally, we use empirical orthogonal functions (EOFs) to analyze the time series of results globally. This technique has been successfully applied to GRACE data for many applications, for example *Wouters and Schrama* [2007]. Figure 5 shows the first (Figures 5a, 5c, 5e, and 5g) and second (Figures 5b, 5d, 5f, and 5h) modes for hydrology and ice signals, which together account for 82% of the variance (the first mode accounts for 69% and the second mode accounts for 13%). The EOFs were constructed using 27 13-day solutions spanning the year. The time series are shown in Figures 5a and 5b followed by the spatial representations of the truth signal (Figures 5c and 5d), recovered signals using two satellite pairs (Figures 5e and 5f), and recovered signals using one satellite pair (Figures 5g and 5h). The one-pair solutions have been destriped and smoothed with a 300 km averaging radius. The two pair solutions have been destriped via a modified destriping algorithm (referred to as D*). It was discovered that correlated errors in spherical harmonic coefficients lead to spurious errors at latitudes greater than 72°, where there is only North-South information in the observable. These errors can be seen spatially in Antarctica in Figure 3b. It was found that if the destriping algorithm described by *Swenson and Wahr* [2006] was applied to coefficients with $3 \leq m \leq 14$ and $n \geq 40$, correlated errors at high latitudes are removed with minimal effect on signals at lower latitudes. Including this step in the analysis generally improves the EOF results (by removing correlated errors at high latitudes), due to the global nature of this technique.

[19] The EOF analysis shown in Figure 5 shows that two pairs of satellites more accurately determine the first two modes both temporally and spatially. Perhaps most impressive is the ability of two satellite pairs to accurately resolve annual mass variations on much finer spatial scales than one satellite pair. A visual inspection of the recovered modes (particularly for the second mode) reveals small-scale hydrology signals in each continent (i.e. Alaska, central Africa, India, Australia) that are detected using two satellite pairs which are either not detected, or smoothed over, using one pair of satellites.

[20] As a summary, in an effort to perform consistent analysis, all remaining results presented in this paper will be post-processed via the following: all gravity solutions are truncated at degree 60; for the case of one pair of satellites we destripe via *Swenson and Wahr* [2006] and perform Gaussian smoothing with an averaging radius of 300 km, and for the case of two satellite pairs we do not perform any post-processing procedures. While the modified destriping algorithm is effective for the EOF analysis due to its global nature, it is not implemented in the regional analysis presented in section 4.

4. Results: A Regional Perspective

4.1. Performance Metrics

[21] As with the processes designed to reduce correlated errors in the gravity solutions, there are a host of methods one can use to perform regional analysis. The two techniques utilized in this paper are averaging kernels [*Swenson and Wahr*, 2002] and spatiospectral localization [*Wieczorek and Simons*, 2005; *Simons et al.*, 2006].

4.1.1. Averaging Kernels

[22] Averaging kernels are traditionally used to quantify mass variations in a region of interest over a specified amount of time. From *Wahr et al.* [1998], a local change in surface mass density for a certain colatitude (θ) and longitude (φ), is given by

$$\Delta\sigma(\theta,\phi) = \frac{a\rho_E}{3}\sum_{l=0}^{\infty}\sum_{m=0}^{l}\frac{2l+1}{l+k_l}\overline{P}_{lm}(\cos\theta) \times \left(\Delta\overline{C}_{lm}\cos m\phi + \Delta\overline{S}_{lm}\sin m\phi\right). \quad (2)$$

In this equation, a is the radius of the Earth, ρ_E is the average density of the solid Earth, k_l are the load love numbers, $\overline{P}_{lm}$ are the normalized associated Legendre functions, and $\overline{C}_{lm}$ and $\overline{S}_{lm}$ are the normalized spherical harmonic coefficients. From *Swenson and Wahr* [2006], we can define an exact averaging kernel to represent the shape of a basin, given by

$$\vartheta(\theta,\phi) = \begin{cases} 0 \text{ outside the basin} \\ 1 \text{ inside the basin} \end{cases} \quad (3)$$

Using this definition, equation (2) can be rewritten to represent the average surface mass density over a region by

$$\overline{\Delta\sigma}_{region} = \frac{a\rho_E}{3\Omega_{region}}\sum_{l=0}^{\infty}\sum_{m=0}^{l}\frac{2l+1}{1+k_l}\left(\vartheta^c_{lm}\Delta\overline{C}_{lm} + \vartheta^s_{lm}\Delta\overline{S}_{lm}\right), \quad (4)$$

where Ω is the area of the region, and ϑ^c_{lm} and ϑ^s_{lm} are the spherical harmonic coefficients describing ϑ (θ, φ). In practice, one would not sum l to ∞, but rather would truncate at some specific degree, l_{trunc}. Truncating introduces an error, as not including all values of l results in an inaccurate representation of the basin shape, and causes ringing around the boundaries of the basin known as the Gibbs phenomenon. Alternately, one can define an

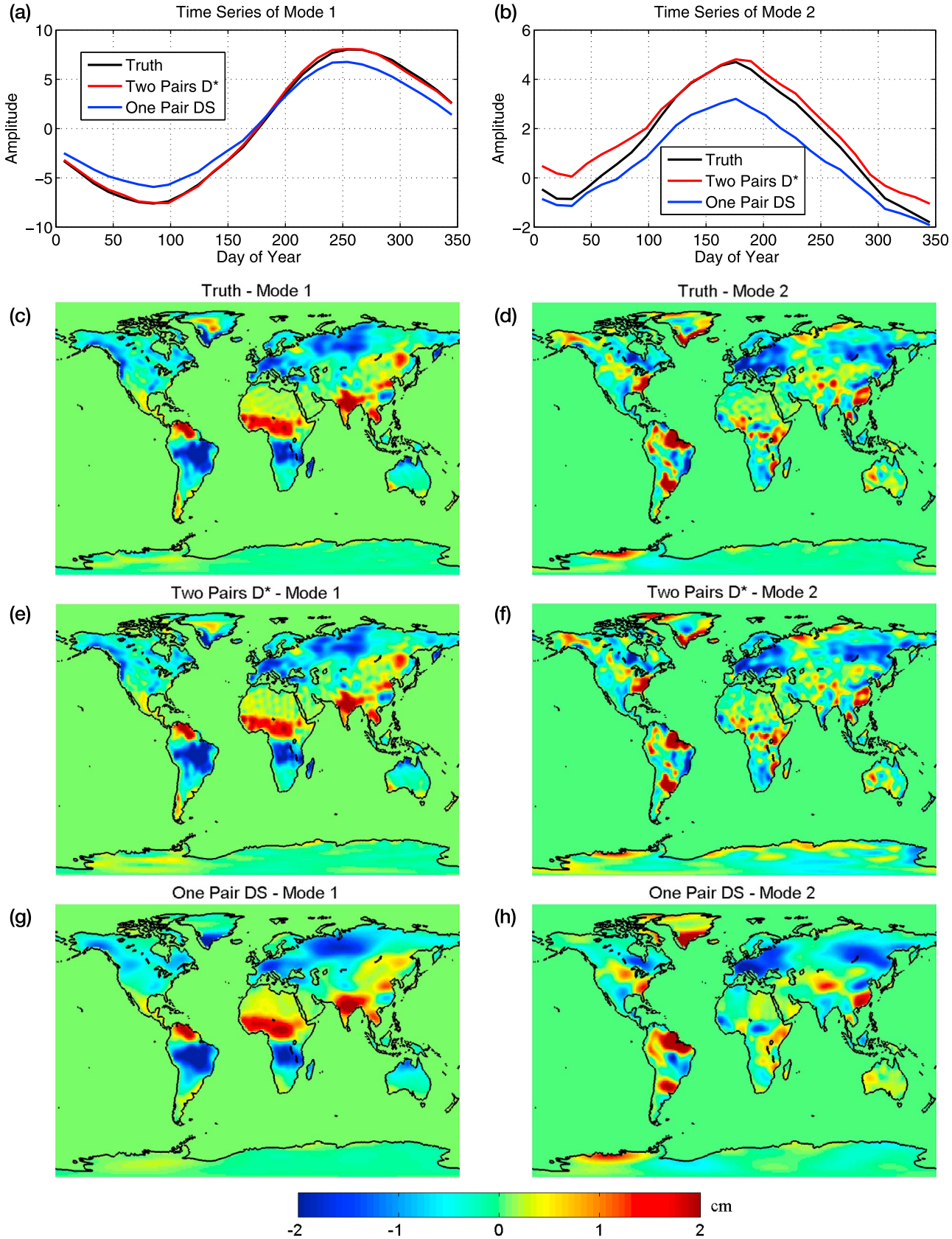

Figure 5. EOF analysis for recovering hydrology and ice signals. Shown are mode 1 and mode 2 with the (a and b) time series, (c and d) truth signal, (e and f) recovered signal using two pairs with modified destriping, and (g and h) recovered signal using one pair with destriping and 300 km smoothing. Units are in cm of EWH.

approximate averaging kernel, W, by replacing ϑ^c_{lm} and ϑ^s_{lm} in equation (4) with W^c_{lm} and W^s_{lm}. This new kernel can be computed a variety of ways; *Swenson and Wahr* [2002] compute it using Gaussian smoothing as well as with a Legendre multiplier method. The drawback to introducing an approximate averaging kernel, given by W, is that while it does decrease truncation error by suppressing short wavelength coefficients, it introduces leakage error into the solution. For our analysis, given the case of smoothing the solutions obtained from one pair of satellites, we use a 300 km Gaussian averaging radius to compute W for the basins of interest. For the case of two satellite pairs, we use exact averaging kernels to eliminate leakage error since the solutions do not necessitate smoothing. While there will be truncation error with this approach, analysis by *Swenson and Wahr* [2002] indicates it will be minimal based on the fact that the smallest basin analyzed is one in Greenland with a size of approximately 100,000 km^2, corresponding to about $l = 60$. The majority of the other basins analyzed are substantially larger than this (see Tables 2 and 3).

4.1.2. Spatiospectral Localization

[23] The principle behind spatiospectral localization is simply to apply an isotropic windowing function that maximizes the ratio of energy of the function within the defined region of interest to that of the entire sphere to obtain a localized representation of the signal. In general, we wish to solve for a localized version ($y(\Omega)$) of a global signal ($f(\Omega)$) given by the following

$$y(\Omega) = h(\theta) f(\Omega), \tag{5}$$

where $h(\theta)$, is an optimal zonal windowing function. The spherical harmonic coefficients describing $y(\Omega)$ are given by *Wieczorek and Simons* [2005] as

$$y_{lm} = \sum_{j=0}^{L_h} \sum_{i=|l-j|}^{l+j} h_j f_{im} \sqrt{(2i+1)(2j+1)(2l+1)} \times (-1)^m \begin{pmatrix} i & j & l \\ 0 & 0 & 0 \end{pmatrix} \begin{pmatrix} i & j & l \\ m & 0 & -m \end{pmatrix}. \tag{6}$$

The matrix symbols in parentheses in equation (6) are Wigner 3-j functions [*Messiah*, 1962]. The only unknown parameter in equation (6) is the term h_j which are the coefficients of the windowing function, and it is left to the user to define an optimal set. *Wieczorek and Simons* [2005] elaborate on how to choose an optimal windowing function. It is done by maximizing the value λ, which defines the ratio of energy of the function within the region of interest (whose area is given by Ω_o) to the energy over the entire sphere, given by

$$\lambda = \int_{\Omega_o} h^2(\Omega) d\Omega \Big/ \int_{\Omega} h^2(\Omega) d\Omega. \tag{7}$$

[24] The solution for λ is attained by solving for the eigenvalues of a matrix given by *Wieczorek and Simons* [2005, equation 13]. The matrix ultimately depends on user-selected values for the radius of the spherical cap, θ_o, along with the maximum degree of expansion, L_h. These values should be selected such that L_o is close to 2, since typically $L_o - 1$ gives the number of well-concentrated windows, where L_o (the Shannon number) is given by [*Han and Ditmar*, 2008]

$$L_o = (L_h + 1)\frac{\theta_o}{\pi}. \tag{8}$$

[25] This technique has been shown to be particularly useful for examining mass variations with large spatial scales in addition to recovering earthquake signals [*Han and Ditmar*, 2008]. In this paper, we apply it to estimating hydrology in the Amazon river basin, ocean bottom pressure signals, as well as a simulated earthquake signal. We calculate localized degree-RMS plots using the calculated coefficients, y_{lm}, and as such, can calculate a localized signal-to-noise ratio (SNR). This is explained in detail by *Han and Ditmar* [2008]. For more details on the spatiospectral localization technique, the reader is referred to *Wieczorek and Simons* [2005] and *Simons et al.* [2006].

4.2. Hydrology

[26] The Amazon river basin has been the subject of many analyses using GRACE data due to the magnitude of the signal as well as the large spatial extent of the region. This region makes an excellent candidate to compare the capabilities of the one-pair and two-pair architectures using the spatiospectral localization technique. A spherical harmonic expansion of degree $L_h = 10$ with a spherical cap radius of $\theta_o = 45°$ is used to calculate the optimal windowing function. The results from a single 13-day gravity solution are displayed in Figure 6, showing the truth signal (Figure 6a), and recovered signals from two pairs (Figure 6b), one pair (Figure 6c), and one pair destriped and smoothed (Figure 6d).

[27] Visually, one can see the improved spatial resolution that two pairs of satellites allow for in this region over one pair. As expected, the one pair results contain longitudinal stripes, and once these solutions are destriped and smoothed, the signals are damped and much of the finer spatial resolution is lost. Figure 7 shows the localized SNR computed from a localized degree-RMS plot. It is seen that for two pairs of satellites, the SNR is positive out to degree 50, corresponding to a spatial resolution of approximately 400 km. Alternately, for the case of one pair of satellites, information is only present out to degrees 30–40, corresponding to spatial resolutions of 500–667 km. Furthermore, the SNR for two satellite pairs is substantially higher than for the case of one pair for all degrees higher than 8, allowing for greater accuracy in determining the signal. It is also seen that the destriping and smoothing processes significantly dampen the signal in the degree bandwidth 15–25.

[28] Next, we use averaging kernels to calculate mass variations over the year in 53 different hydrological basins shown in Figure 8. This selection of basins represents different basin sizes, latitudes, geographic orientations, signal strengths, etc, and gives a good sampling on the type of performance one could hope to achieve with two pairs of satellites over one pair of satellites. Figure 9 focuses on the results for the Fraser Basin (Basin 18), in northwestern British Columbia. Mass variations for this analysis were calculated each day using a sliding boxcar filter with a window width of 13 days centered on the day of interest. Each solution has approximately the same spatial information in it, given that the orbits are in repeating ground tracks; however, it has different space-time sampling

characteristics. Note that these solutions are not true "daily" solutions in the sense that solutions between days are independent from one another. In fact, independent solutions will happen every 13 days. It is also not being argued that this type of filter is optimal for recovering mass variations each day, as other filters have been explored for this purpose, including using a Gaussian filter similar to the boxcar filter that we use [*Bonin*, 2010], as well as using a Kalman filter during the estimation process to gain daily solutions [*Kurtenbach et al.*, 2009]. This simple analysis, however, allows one to see the variability in the solutions resulting from replacing a single day of data.

[29] Figure 9 illustrates the calculated mass variations over the year using an averaging kernel for Basin 18, the Fraser Basin. Shown are the solution for one pair of satellites with no post-processing, the one-pair solution that has been destriped and smoothed, the one-pair solution that has been destriped and smoothed with a scale factor (SF) applied, and the two-pair solution. Scale factors are used within the GRACE community to account for signal that the destriping and smoothing processes remove from the solution. Typically, they are calculated by taking a model representing mass variations in the region, destriping and smoothing that model, and calculating how much mass has been removed via these processes. A scale factor is then calculated to restore this lost mass. For this study, we calculated scale factors three ways: (1) using the *truth* GLDAS hydrology model, (2) using an alternate hydrology model provided by the European Space Agency (ESA), and (3) using a uniform mass distribution over the basin. It was found that the scale factor computed was extremely sensitive to which method was used due to the empirical nature of the destriping filter. In fact, using a scale factor from methods (2) and (3) provided worse results on average than not using a scale factor at all. Thus, it was decided to compute scale factors using method (1): destriping and smoothing the *truth* model. This leads to overly-optimistic results for the case of one pair of satellites, as it represents the best possible scale factor one could hope to compute. Hence, the actual level of mass variations for one pair of satellites that one would compute most likely lies somewhere between the case of not applying any scale factor, and the case of applying the best possible scale factor.

[30] Figure 9 shows that the signal calculated using one pair of satellites without post-processing has large variability, changing by as much as 15 cm EWH from one time step to the next. Once the solution is destriped and smoothed, the variability in the solution decreases substantially; however, the signal is damped in amplitude with respect to the truth signal. Figure 8 illustrates that the Fraser Basin is predominantly oriented in the North-South direction. As such, the destriping process removes a substantial amount of signal (in addition to error) from the basin since the empirical filter developed by *Swenson and Wahr* [2006] is designed to remove North-South features. After applying the scale factor to account for this loss of signal, the one-pair solution compares fairly well with the truth signal. The solution obtained from two pairs of satellites, however, still agrees much better with the truth signal than the best-case scenario involving one pair of satellites, with the red curve almost completely overlying the black curve. The reader should be reminded, as well, that no post-processing has been applied to the solution involving two pairs of satellites.

[31] Table 2 shows the RMS of the errors (in cm of EWH) calculated over the year for the Fraser Basin in addition to the other 52 basins that were analyzed. Listed are the name of each basin, the area, the amplitude (amp.) of the signal in the basin over one full year (taken to be half of the peak-to-peak amplitude), as well as the RMS of the error for each case. Note that 'Reg.' stands for regular processing (i.e. no post-processing).

[32] Studying the RMS values in Table 2 shows that in all but four of the basins, two pairs of satellites has a lower RMS than for the case of one pair of satellites being destriped and smoothed with an optimal scale factor applied. It has a lower RMS than the one-pair case with no post-processing 100% of the time. Furthermore, if one looks at the effect of applying the scale factor, it is seen that in some cases, the scale factor actually makes the solution slightly worse. This indicates the risks that one takes by applying scale factors to the mass estimates. Even given an optimal scale factor, the results sometimes degrade. Taking the RMS of the RMS of each basin (seen in the last row of Table 2), it can be concluded that two pairs of satellites determines the hydrological mass variations in the basins with approximately 25% more accuracy than the case of one pair of satellites destriped and smoothed with an optimal scale factor applied, 40% more accuracy than the case of one pair of satellites destriped and smoothed with no scale factor applied, and 80% more accuracy than in the case of one pair of satellites with no post-processing.

4.3. Ice Mass Variations

[33] Ice mass variations in this paper are defined as mass variations in Greenland and Antarctica. In order to study ice mass variations on a regional scale, Greenland has been subdivided into 12 basins, as shown in Figure 10, in accordance with basin definitions given by *Luthcke et al.* [2006]. The melting of Greenland around the coastal areas, particularly the southern regions, has been the focus of many recent investigations due to accelerating ice mass loss. As such, detailed simulation results for mass variations in Basin 5, along the southwestern coast of Greenland, are shown in Figure 11.

[34] Figure 11 paints a similar picture as that of the Fraser basin shown in Figure 9. The solution from one pair of satellites is quite noisy; however, once the solutions are destriped and smoothed, the daily variability has decreased and the amplitude of the signal has been suppressed with respect to the truth. This is in a large part due to the North-South orientation of this particular basin, and the fact that the destriping process is designed to remove North-South features in the gravity field. Once an optimal scale factor is applied, the amplitude has been restored and the calculated mass matches much closer to the truth. However, particularly for the first half of the year, there is a poor estimate of the rate of mass increase. The mass variations calculated with two pairs of satellites, conversely, recovers the true mass variations in the basin accurately for the duration of the year.

[35] Table 3 shows the calculated error RMS values for all 12 Greenland basins over the year. In all but 2 of the basins, two pairs of satellites provide lower RMS values

Table 2. RMS of the Error, in cm of EWH, in Determining Mass Variations in the Hydrological Basins Over One Year[a]

Basin	Basin Name	Area (km^2)	Amp. (cm)	One Pair RMS (cm)			Two Pairs RMS (cm)
				Reg.	DS	DS/SF	
1	Khatanga-Popigai	501,552	6.58	5.68	1.68	1.26	0.66
2	Olenek	309,322	2.83	4.24	1.69	1.00	0.82
3	Lena	2,415,920	3.51	1.56	0.78	0.79	0.78
4	Yana	242,039	2.97	11.26	1.54	1.29	0.98
5	Indigirka	341,076	3.33	10.95	1.51	1.99	1.23
6	Yenisei	2,376,483	4.38	2.32	0.81	0.79	0.64
7	Kolyma	617,341	5.51	5.19	2.09	1.83	1.53
8	Taz	382,104	10.87	7.26	1.36	1.08	0.79
9	Mackenzie	1,770,040	4.53	1.26	1.01	0.92	0.63
10	Pechora	254,272	10.52	7.06	1.65	1.29	1.24
11	Ob	3,012,693	7.59	1.32	0.91	0.92	0.74
12	Severnaya Dvina	661,781	10.91	1.79	1.22	0.98	0.89
13	Anadyr	410,068	5.12	6.57	2.02	1.46	1.26
14	Yukon	940,852	5.90	2.47	1.42	1.39	0.95
15	Nelson	1,693,827	4.18	1.54	0.67	0.62	0.52
16	Ural	312,629	5.35	4.92	1.07	1.14	1.09
17	Amur	2,876,880	3.87	1.28	0.82	0.85	0.63
18	Fraser	357,057	11.15	6.04	4.14	1.83	0.77
19	Saint Lawrence	1,263,145	6.04	1.63	1.21	1.20	0.47
20	Volga	1,580,750	6.17	1.41	0.94	0.91	0.65
21	Dnieper	446,335	8.34	2.85	1.21	1.15	0.73
22	Don	278,565	7.21	6.75	2.21	1.96	1.05
23	Columbia	1,048,534	6.56	2.79	1.95	1.07	0.63
24	Danube	836,815	10.47	2.23	1.76	1.19	0.64
25	Yellow River	1,872,050	4.12	1.40	0.88	0.91	0.66
26	Colorado (U.S.)	838,512	1.32	2.65	0.83	0.93	0.79
27	Yangtze River	1,833,747	4.34	1.56	0.92	0.93	0.62
28	Mississippi	3,525,101	4.19	0.90	0.53	0.53	0.46
29	Nile	3,761,542	3.54	1.94	0.92	0.96	0.57
30	Shatt al-Arab	1,732,018	2.39	2.11	0.95	1.04	0.64
31	Rio Grande	1,021,678	3.54	2.37	1.05	1.49	0.85
32	Indus	1,429,312	3.19	2.17	1.05	1.18	0.70
33	Ganges	1,920,796	10.12	1.53	1.23	0.82	0.62
34	Pearl River	439,492	9.22	3.64	1.42	1.33	1.30
35	Irrawaddy	296,014	3.94	8.54	2.14	0.91	1.89
36	Salween	1,014,279	2.63	3.67	1.48	1.35	0.93
37	Sénégal	765,749	3.49	2.47	0.99	0.91	1.25
38	Mekong	743,472	11.34	3.01	2.91	1.63	1.26
39	Orinoco	1,255,019	10.04	1.99	1.28	1.08	0.95
40	Magdalena	195,874	9.59	8.76	2.69	2.01	1.81
41	Volta	572,618	12.17	3.24	1.43	1.15	1.14
42	Niger	6,918,253	4.83	0.97	0.74	0.70	0.39
43	Jubba	627,755	4.63	3.05	0.99	1.18	1.14
44	Amazon	6,129,528	8.11	0.97	0.82	0.74	0.49
45	Tocantins	1,011,450	18.44	3.62	3.22	2.09	1.29
46	Zaire	4,449,039	3.57	1.02	0.92	0.91	0.56
47	São Francisco	904,455	8.89	3.26	1.59	1.62	1.18
48	Victoria	816,232	7.90	3.50	1.12	1.12	1.14
49	Zambezi	2,351,974	10.18	1.19	1.32	0.84	0.52
50	Oranje	891,596	2.15	2.03	1.66	1.66	0.80
51	Paraná	3,635,738	7.38	1.34	1.40	1.10	0.48
52	Murray	2,452,8734	2.63	1.92	1.06	1.09	0.76
53	Colorado (Argentina)	659,923	3.46	4.54	0.89	1.01	1.16
	RMS of RMS			4.22	1.55	1.23	0.94

[a]Reg = no post-processing, DS = destriped and smoothed, DS/SF = destriped and smoothed with an optimal scale factor applied.

than the best case scenario using one pair of satellites. Two pairs of satellites provides lower RMS values 100% of the time over what one pair of satellites provides with no post-processing. It is also interesting to note that the basins in the southern half of Greenland (Basins 4, 5, 10, and 11) which get coverage from both pairs of satellites have a larger signal-to-noise ratio than the basins in the northern half of Greenland (Basins 1, 2, 7, and 8) which get coverage from only the polar pair of satellites. Again, it should be noted that applying an optimal scale factor does not always guarantee a better solution for the case of one pair of satellites, indicating that care must be taken when applying scale factors to real data.

[36] By calculating the RMS of the yearly error RMS values (displayed in the last row of Table 3), it can be concluded that on average, two pairs of satellites provides mass estimates for Greenland that are approximately 55% more accurate than in the case of one pair of satellites that have been destriped and smoothed with an optimal scale factor applied, 75% more accurate than in the case of one

Table 3. RMS of the Error, in GT of Ice, in Determining Mass Variations in the Greenland Basins Over One Year[a]

Basin	Area (km^2)	Amp. (GT)	One Pair RMS (GT)			Two Pairs RMS(GT)
			Reg.	DS	DS/SF	
1	207,331	11.36	4.63	5.56	6.26	2.83
2	225,127	6.97	9.77	4.19	7.49	2.73
3	178,723	17.14	21.04	5.23	3.29	3.31
4	109,816	34.34	7.03	12.37	1.97	1.21
5	194,759	70.35	17.86	34.52	9.63	2.82
6	149,417	14.72	17.64	7.91	6.51	2.06
7	103,225	3.14	3.63	3.15	5.01	2.10
8	190,789	4.18	9.57	4.79	12.05	4.77
9	191,186	11.02	28.12	2.94	3.21	4.08
10	146,600	23.84	14.31	3.36	3.41	2.06
11	196,199	22.95	21.32	4.87	4.49	2.46
12	235,481	9.97	21.06	8.78	9.74	3.66
	RMS of RMS		16.43	11.68	6.78	2.99

[a]Reg = no post-processing, DS = destriped and smoothed, DS/SF = destriped and smoothed with an optimal scale factor applied.

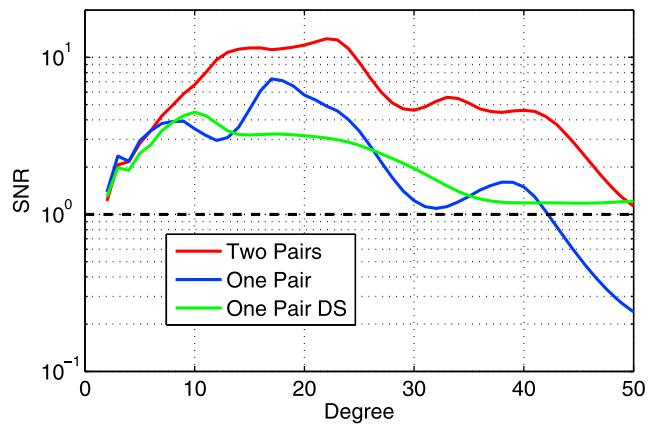

Figure 7. Signal-to-noise ratio for mass variations in the Amazon computed with the spatiospectral localization technique (see Figure 6).

pair of satellites that have been destriped and smoothed without applying a scale factor, and 80% more accurate than in the case of one pair of satellites with no post-processing. The reason that the magnitude of the RMS values in Table 3 are substantially larger than those associated with hydrology in Table 2 can be attributed to three factors. First, as was shown by *Loomis* [2009], temporal aliasing errors from atmosphere and ocean dealiasing (AOD) products in Greenland are larger than AOD errors over areas such as the Amazon, or North America, where there are substantially more data available as input for the models. Second, high degree resonant order coefficients manifest themselves spatially between 70° and 75°, which is where Greenland lies [*Wiese*, 2011]. Particularly for the case of a single pair of satellites, the errors at high degree resonant coefficients are high, as seen in Figure 2c, and as such, there is a substantial amount of error at this latitude band. Finally, the amplitude of the signal in Greenland is, on average, larger than the amplitude

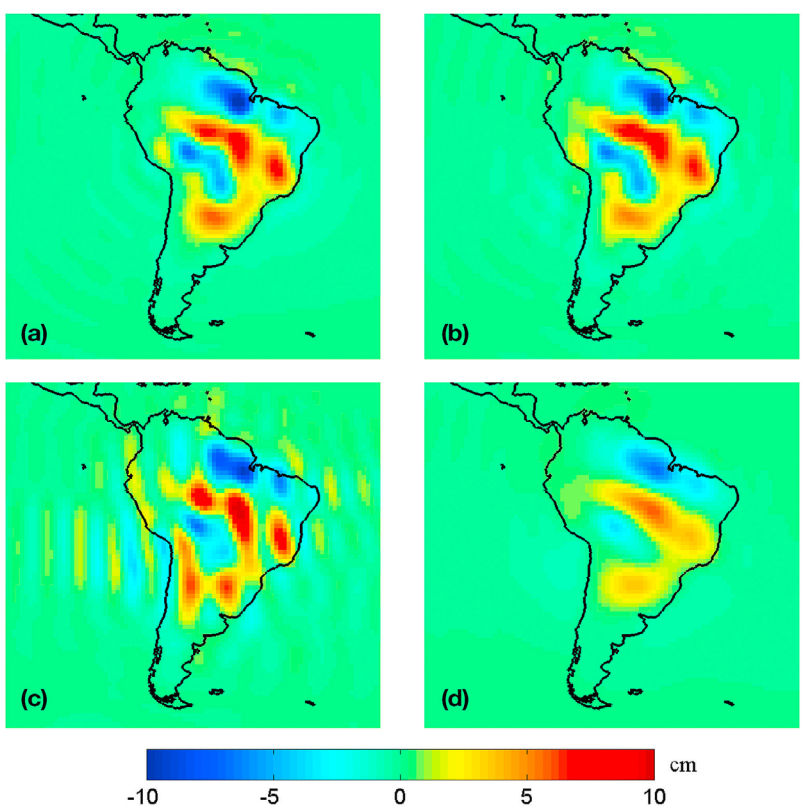

Figure 6. Spatiospectral localization technique applied to the Amazon region using $\theta_o = 45°$, $L_h = 10$. (a) Truth signal along with the recovered signals from: (b) two pairs of satellites, (c) one pair of satellites, and (d) one pair of satellites DS averaged over 13 days. Units are in cm of EWH.

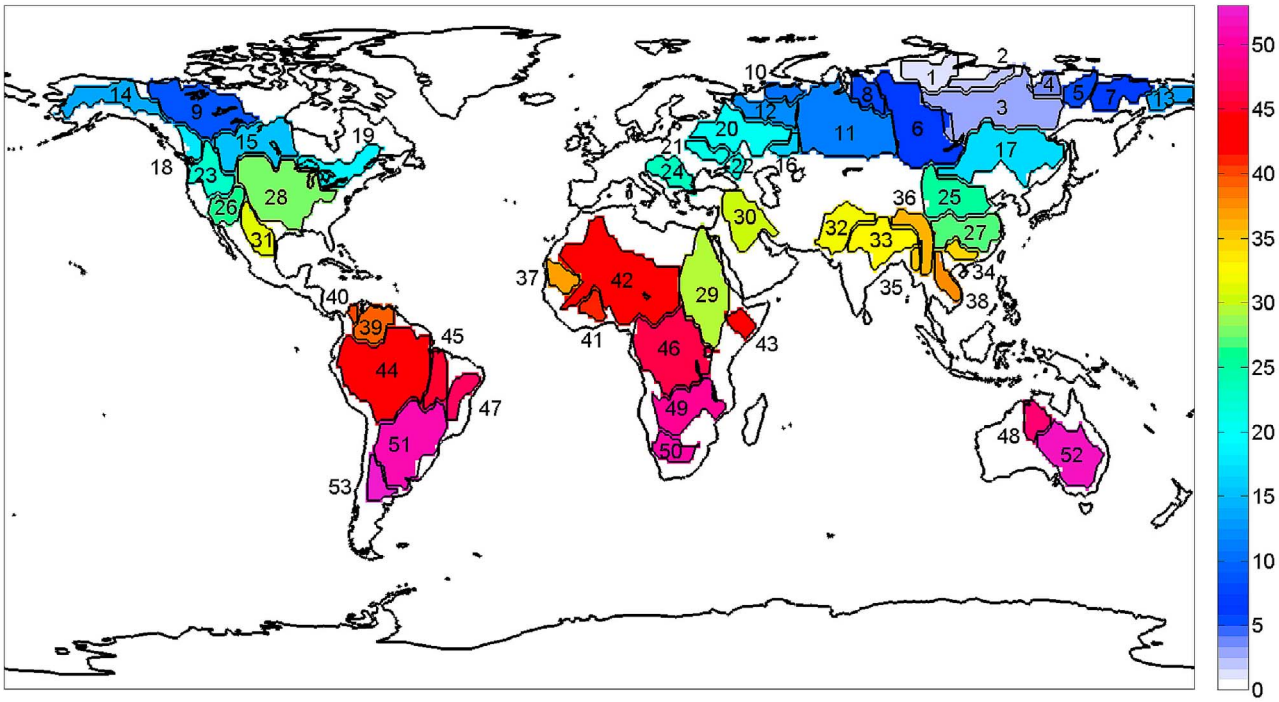

Figure 8. Map showing the location of the 53 hydrological basins for which averaging kernels are computed.

of the continental hydrology signals. Hence, larger absolute errors in determining ice mass variations in Greenland lead to similar signal-to-noise ratios between the two types of signals.

4.4. Ocean Bottom Pressure Signals

[37] Ocean bottom pressure (OBP) signals are, on average, much larger in spatial scale and smaller in magnitude than hydrology or ice signals. The smaller magnitude of the signals indicates that OBP signals will have a smaller SNR when recovering them than hydrology and ice mass variations, making them more difficult to detect. As a result of this, OBP signals have been more difficult to quantify using GRACE, and regional analyses of the data have been limited to a handful of studies. In this analysis, we use spatiospectral localization to analyze OBP signals in the Southeast Pacific Basin. This particular basin is of interest due to high variability in the OBP signals, primarily due to topographically trapped signals. Figure 12 illustrates the dipole signal in the Southeast Pacific Basin via spatiospectral localization using a spherical cap radius of $\theta_o = 25°$ and maximum degree of expansion $L_h = 15$. Shown are the 13-day average of the

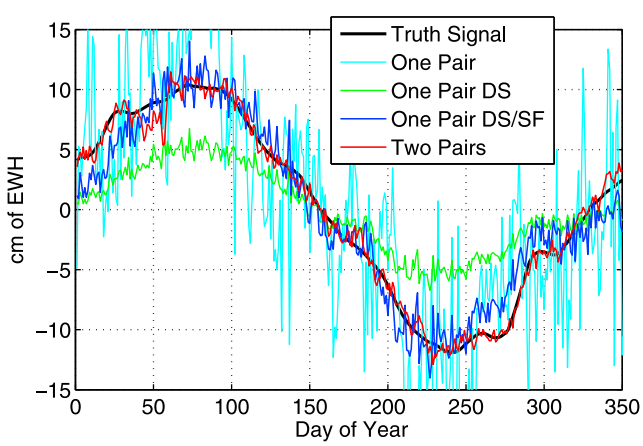

Figure 9. Mass variations calculated in the Fraser Basin (Basin 18) over the year for one pair of satellites, one pair of satellites DS, one pair of satellites DS with a scale factor applied, and for two pairs of satellites.

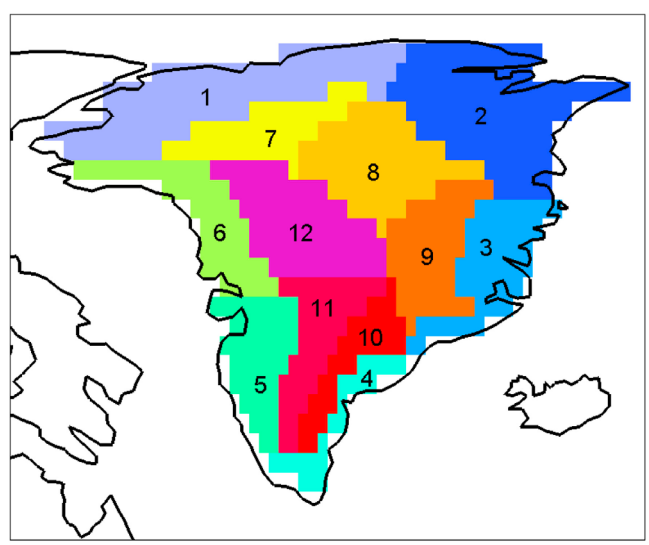

Figure 10. Map showing the location of the 12 Greenland basins.

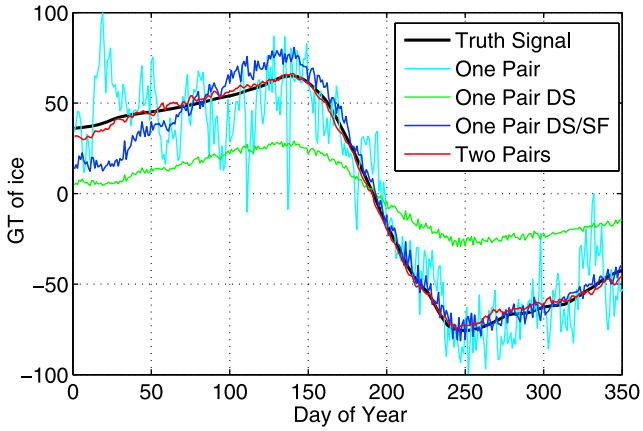

Figure 11. Mass variations calculated in southwestern Greenland (Basin 5) over the year for one pair of satellites, one pair of satellites DS, one pair of satellites DS with a scale factor applied, and for two pairs of satellites.

truth signal (Figure 12a), and the 13-day averages of the recovered signal using two satellite pairs (Figure 12b), one pair (Figure 12c), and one pair destriped and smoothed (Figure 12d), expressed in cm of EWH.

[38] Figure 12 shows that two pairs of satellites recover this signal particularly well. The signal is not discernible with one pair of satellites and no post-processing. Once the solutions are destriped and smoothed, the negative part of the dipole signal is present, although distorted spatially, while the positive part is faintly present in the solution. Figure 13 illustrates the SNR as a function of spherical harmonic degree of the three cases. The solution obtained with two pairs of satellites has a positive SNR out to approximately degree 35, while the destriped and smoothed solution using one pair of satellites has information until approximately degree 25 or so. This represents an improvement in spatial resolution from 800 km to 571 km in determining this particular signal.

[39] Finally, we analyze mass variations over the year in this basin (boundaries given by 90°–140°W, 35°–55°S, as defined by *Boening et al.* [2011]) using an averaging kernel. Figure 14 shows the ability of each architecture to recover OBP variations in the Southeast Pacific Basin. Figure 14 shows excellent agreement between the truth signal and the recovered signal using two pairs of satellites, particularly during times of high variability, with the red curve nearly completely overlying the black curve. The RMS of the error is decreased by over 70%, from 0.36 cm to 0.10 cm, with the addition of the second pair of satellites. One pair of satellites fails to capture much of the high frequency variability in OBP in this region.

4.5. Earthquakes

[40] GRACE has been used effectively to determine coseismic and postseismic gravity deformations due to

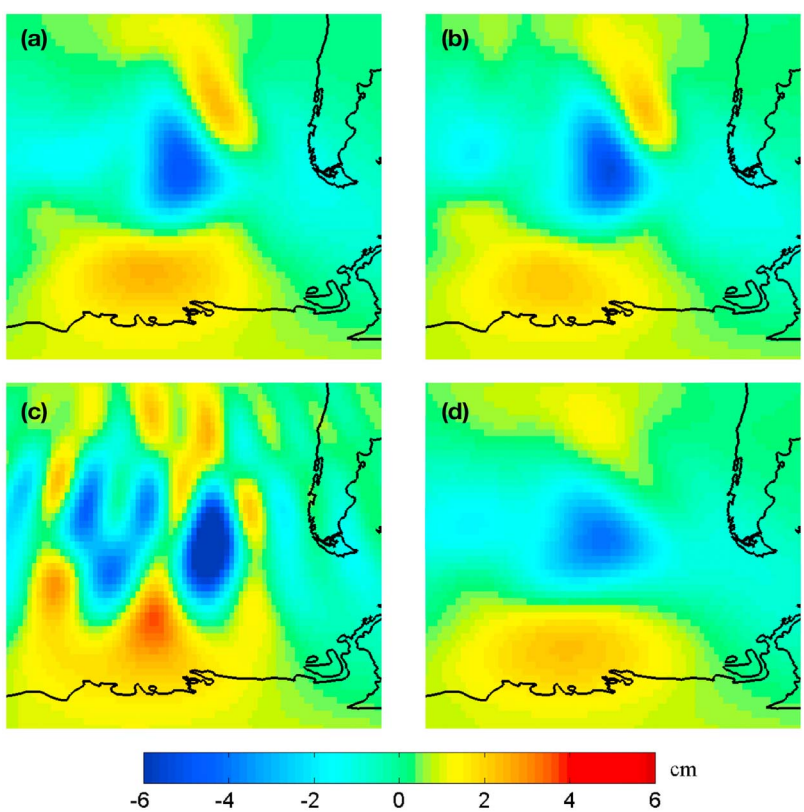

Figure 12. Spatiospectral localization technique applied to the Southeast Pacific Basin using $\theta_o = 25°$, $L_h = 15$. (a) Truth signal along with the recovered signals from: (b) two pairs of satellites, (c) one pair of satellites, and (d) one pair of satellites DS averaged over 13 days. Units are in cm of EWH.

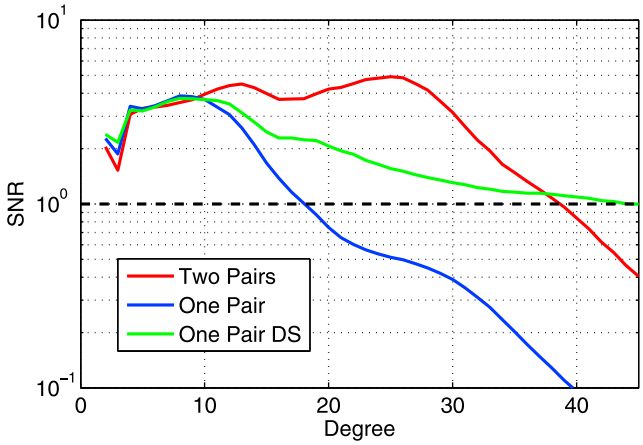

Figure 13. Signal-to-noise ratio for OBP signals in the Southeast Pacific Basin computed using spatiospectral localization (see Figure 12).

earthquakes, in particular the 2004 Sumatra-Andaman earthquake [*Chen et al.*, 2007; *Panet et al.*, 2007; *Han and Simons*, 2008] and the 2010 Maule, Chile earthquake [*Han et al.*, 2010; *Heki and Matsuo*, 2010]. It is our goal to quantify the expected performance that two satellite pairs offers in sensing the coseismic part of the earthquake signal via spatiospectral localization. To perform this simulation, we use an earthquake model representative of the magnitude 8.8 2010 Maule, Chile earthquake (available from the U.S. Geological Survey, http://earthquake.usgs.gov). This model is introduced in the *truth* set of models as a step function that is added to the static gravity field model, EIGEN-GL04C, and is then recovered in addition to the hydrology and ice signals. We apply an optimal windowing function with $\theta_o = 25°$ and $L_h = 15$ to analyze the signal. Figure 15 shows the modeled earthquake signal (Figure 15a), the recovered signal using two satellite pairs (Figure 15b), the recovered signal using one pair of satellites (Figure 15c), and the recovered signal if the single satellite pair solution is destriped and smoothed (Figure 15d). The plots are expressed in cm of EWH. It should be noted that the positive mass anomaly in the upper-right part of the truth signal is actually a hydrology signal in the Paraná Basin that has been captured by the windowing function which is applied. It could be removed via forward modeling to isolate the earthquake signal, but this was deemed unnecessary for the purposes of this study. Figure 16 illustrates the localized SNR associated with the recovered earthquake signal.

[41] It is seen that while two pairs of satellites does an exceptional job of recovering the signal with a high SNR out to degree 45, one pair of satellites is equally capable of recovering the signal, although with a lower SNR. It is expected that two pairs of satellites will be able to recover earthquakes lower in magnitude than what one pair of satellites can recover. The threshold of recovery will depend on the location of the earthquake, the magnitude of the earthquake, as well as the type of earthquake. An extensive set of simulations varying the size, strength, and type of earthquake is necessary to characterize a detection threshold that two pairs of satellites offers over one pair. This analysis is not presented in this paper; however, we have shown that large earthquakes, such as the 2010 Maule, Chile earthquake can be detected with much greater accuracy using two pairs of satellites over one pair of satellites.

5. Conclusions

[42] It is expected that future satellite missions dedicated to recovering temporal gravity variations will be limited in their performance by temporal aliasing errors. An effective way to reduce these errors is by adding a second pair of satellites. Previous studies have shown that a near-optimal architecture involving two dedicated pairs of satellites is obtained when both satellite pairs are in 13-day repeating orbits, one pair in a polar orbit at 320 km and the other pair lower inclined, at 72°, at 290 km. Given this scenario, we show expected improvements in determining continental hydrology, ice mass variations, ocean bottom pressure signals, and earthquake signals. An EOF analysis examining the first two modes reveals that two satellite pairs detects annual variations in small river basins which are undetected using one pair of satellites. Global analysis of results are insufficient, however, as the ability to recover mass variations in a particular region depend on the size of the signal and error, the geographic location, and the space-time sampling characteristics of the satellites. As such, the best one can hope to do to characterize mission performance is to perform realistic numerical simulations to recover mass variations in a variety of regions.

[43] Averaging kernels are used to analyze 53 hydrological basins across the globe as well as 12 basins in Greenland. On average, when no post-processing is applied to the gravity solutions, two pairs of satellites offers an 80% reduction in error in determining mass variations in the basins over the year. After the single satellite pair solutions have been destriped, smoothed, and mass has been restored using an appropriate scale factor, two pairs of satellites (with

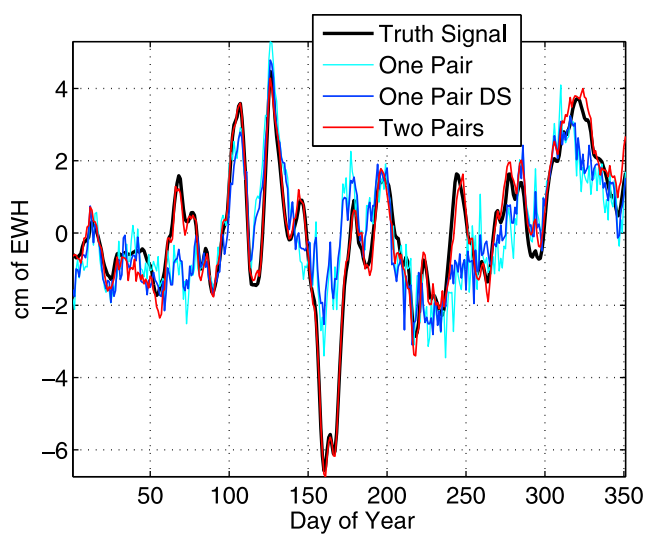

Figure 14. Mass variations in the Southeast Pacific Ocean over the year showing the calculated mass from one pair of satellites, one pair DS, and two pairs of satellites.

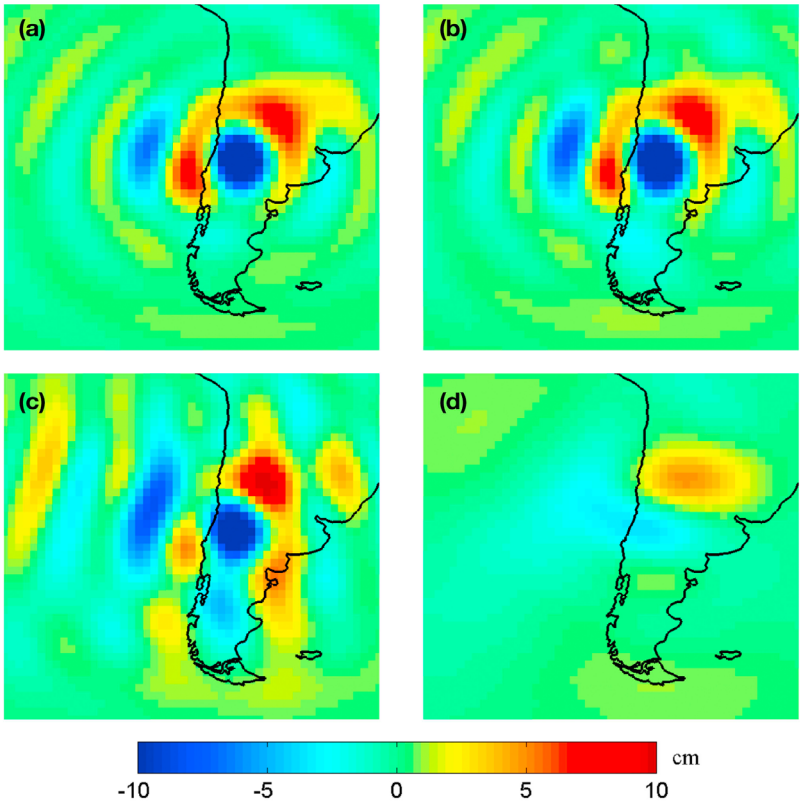

Figure 15. Spatiospectral localization technique applied to recover a simulated signal similar to the 2010 Maule, Chile earthquake, using $\theta = 25°$, $L_h = 15$. (a) Truth signal along with the recovered signals from: (b) two pairs of satellites, (c) one pair of satellites, and (d) one pair of satellites DS averaged over 13 days. Units are in cm of EWH.

no post-processing) still, on average, provides a 25%–40% reduction in errors in determining mass variations in the hydrological basins and a 55%–75% reduction in errors in determining mass variations in the Greenland basins over the year. Spatiospectral localization analysis is used to analyze ocean bottom pressure signals in the Southeast Pacific Basin as well as a simulated earthquake signal similar to the 2010 Maule, Chile earthquake. Two pairs of satellites improves the spatial resolution in determining the ocean bottom pressure signal from 800 km to 570 km, and determines the total mass in the basin over the year with 70% more accuracy than one satellite pair. While the earthquake signal is detected using both architectures, two pairs of satellites increases the signal-to-noise ratio at higher degrees by approximately one-half of an order of magnitude. It is expected that the addition of a second pair of satellites will also allow for earthquakes smaller in magnitude to be quantified which otherwise would be undetected with gravity measurements.

[44] Perhaps the largest advantage of adding a second pair of satellites is that the solutions do not necessitate ad hoc GRACE post-processing procedures when studying signals to spatial resolution of ~330 km. This eliminates much of the confusion as to what the destriping and smoothing algorithms do to geophysical signals. Additionally, one does not need to worry about applying incorrect scale factors to the solutions when trying to restore mass that the destriping and smoothing processes have removed. The results in this paper are regarded to be relatively pessimistic for the case of two pairs of satellites. It is expected that optimized post-processing techniques will be developed for such an architecture which would increase the spatial resolution in the solutions even further. This, in turn, would allow for mass variations to be determined in smaller river basins than those analyzed in this study.

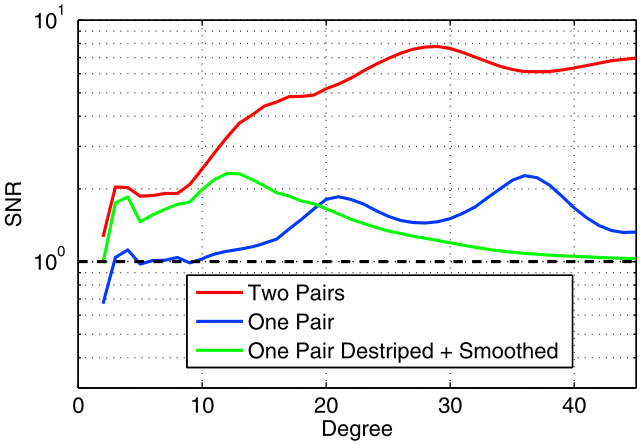

Figure 16. Localized SNR for recovering the simulated 2010 Maule, Chile earthquake (see Figure 15).

[45] **Acknowledgments.** This research was funded by the National Science Foundation Graduate Fellowship Program, the National Defense Science and Engineering Graduate Fellowship Program, and the NASA GRACE Science Team investigation (NNX08AH63G). The authors would like to thank NASA Goddard Space Flight Center for providing GEODYN and SOLVE to perform the numerical simulations, along with the NCEP model. We acknowledge Jean-Paul Boy (EOST/University of Strasbourg, France) for providing the ECMWF-derived and MOG-2D-derived data sets in this study to GSFC. Additionally, we thank the European Space Agency (ESA) and the Institute of Astronomical and Physical Geodesy (IAPG) at the Technical University of Munich for providing the ice model used in the simulations. Jianli Chen from the Center for Space Research at the University of Texas at Austin is acknowledged for providing the hydrology basin definitions while Bryant Loomis of SGT is acknowledged for providing the Greenland basin definitions.

References

Alnis, J., A. Matveev, N. Kolachevsky, T. Udem, and T. W. Hansch (2008), Subhertz linewidth diode lasers by stabilization to vibrationally and thermally compensated ultralow-expansion glass Fabry-Pérot cavities, *Phys. Rev. A*, *77*(5), 053809, doi:10.1103/PhysRevA.77.053809.

Battrick, B. (1999), The four candidate Earth explorer core missions: Gravity field and steady-state ocean circulation mission, Eur. Space Agency Spec. Publ, ESA SP-1233(1), 217 pp.

Bender, P. L., J. L. Hall, J. Ye, and W. M. Klipstein (2003), Satellite-satellite laser links for future gravity missions, *Space Sci. Rev.*, *108*, 377–384, doi:10.1023/A:1026195913558.

Bender, P. L., D. N. Wiese, and R. S. Nerem (2008), A possible dual-GRACE mission with 90 degree and 63 degree inclination orbits, paper presented at Third International Symposium on Formation Flying, Eur. Space Agency, Noordwijk, Netherlands, 23–25 April.

Boening, C., T. Lee, and V. Zlotnicki (2011), A record-high ocean bottom pressure in the South Pacific observed by GRACE, *Geophys. Res. Lett.*, *38*, L04602, doi:10.1029/2010GL046013.

Bonin, J. A. (2010), Improving the observation of time-variable gravity using GRACE RL04 data, Ph.D. dissertation, Cent. for Space Res., Univ. of Tex. at Austin, Austin.

Bruinsma, S., J. M. Lemoine, R. Biancale, and N. Vales (2009), CNES/GRGS 10-day gravity field models (release 2) and their evaluation, *Adv. Space Res.*, *45*(4), 587–601, doi:10.1016/j.asr.2009.10.012.

Carrère, L., and F. Lyard (2003), Modeling the barotropic response of the global ocean to atmospheric wind and pressure forcing, *Geophys. Res. Lett.*, *30*(6), 1275, doi:10.1029/2002GL016473.

Chambers, D. P. (2006), Evaluation of new GRACE time-variable gravity data over the ocean, *Geophys. Res. Lett.*, *33*, L17603, doi:10.1029/2006GL027296.

Chen, J. L., C. R. Wilson, and K. W. Seo (2006), Optimized smoothing of gravity recovery and climate experiment (GRACE) time-variable gravity observations, *J. Geophys. Res.*, *111*, B06408, doi:10.1029/2005JB004064.

Chen, J. L., C. R. Wilson, B. D. Tapley, and S. Grand (2007), GRACE detects coseismic and postseismic deformation from the Sumatra-Andaman earthquake, *Geophys. Res. Lett.*, *34*, L13302, doi:10.1029/2007GL030356.

Colombo, O. (1984), *The Global Mapping of Gravity With Two Satellites, Publ. on Geod.*, vol. 7, Netherlands Geod. Comm., Delft, Netherlands.

Davis, J. L., M. E. Tamisiea, P. Elósegui, J. X. Mitrovica, and E. M. Hill (2008), A statistical filtering approach for gravity recovery and climate experiment (GRACE) gravity data, *J. Geophys. Res.*, *113*, B04410, doi:10.1029/2007JB005043.

Duan, X. J., J. Y. Guo, C. K. Shum, and W. van der Wal (2009), On the postprocessing removal of correlated errors in GRACE temporal gravity field solutions, *J. Geod.*, *83*, 1095–1106, doi:10.1007/s00190-009-0327-0.

Elsaka, B. (2010), Simulated satellite formation flights for detecting the temporal variations of the Earth's gravity field, Ph.D. dissertation, Inst. for Geod. and Geoinf., Univ. of Bonn, Bonn, Germany.

Flechtner, F. (2007), AOD1b product description document for product releases 01 to 04, *GRACE 327–750*, GeoForschungszentrum Potsdam, Potsdam, Germany.

Förste, Ch., et al. (2008), The GFZ/GRGS satellite and combined gravity field models EIGEN-GL04S1 and EIGEN-GL04C, *J. Geod.*, *82*(6), 331–346, doi:10.1007/s00190-007-0183-8.

Guo, J. Y., X. J. Duan, and C. K. Shum (2010), Non-isotropic Gaussian smoothing and leakage reduction for determining mass changes over land and ocean using GRACE data, *Geophys. J. Int.*, *181*, 290–302, doi:10.1111/j.1365-246X.2010.04534.x.

Han, S. C., and P. Ditmar (2008), Localized spectral analysis of global satellite gravity fields for recovering time-variable mass redistributions, *J. Geod.*, *82*, 423–430, doi:10.1007/s00190-007-0194-5.

Han, S. C., and F. J. Simons (2008), Spatiospectral localization of global geopotential fields from the Gravity Recovery and Climate Experiment (GRACE) reveals the coseismic gravity change owing to the 2004 Sumatra-Andaman earthquake, *J. Geophys. Res.*, *113*, B01405, doi:10.1029/2007JB004927.

Han, S. C., C. Jekeli, and C. K. Shum (2004), Time-variable aliasing effects of ocean tides, atmosphere, and continental water mass on monthly mean GRACE gravity field, *J. Geophys. Res.*, *109*, B04403, doi:10.1029/2003JB002501.

Han, S. C., C. K. Shum, C. Jekeli, C. Y. Kuo, C. R. Wilson, and K. W. Seo (2005), Non-isotropic filtering of GRACE temporal gravity for geophysical signal enhancement, *Geophys. J. Int.*, *163*, 18–25, doi:10.1111/j.1365-246X.2005.02756.x.

Han, S. C., J. Sauber, and S. Luthcke (2010), Regional gravity decrease after the 2010 Maule (Chile) earthquake indicates large-scale mass redistribution, *Geophys. Res. Lett.*, *37*, L23307, doi:10.1029/2010GL045449.

Heki, K., and K. Matsuo (2010), Coseismic gravity changes of the 2010 earthquake in central Chile from satellite gravimetry, *Geophys. Res. Lett.*, *37*, L24306, doi:10.1029/2010GL045335.

Jekeli, C. (1981), Alternative methods to smooth the Earth's gravity field, *Rep. 327*, Dep. of Geod. Sci. and Surv., Ohio State Univ., Columbus.

Kalnay, E., et al. (1996), The NCEP/NCAR 40-year reanalysis project, *Bull. Am. Meteorol. Soc.*, *77*, 437–470.

Klees, R., E. A. Revtova, B. C. Gunter, P. Ditmar, E. Oudman, H. C. Winsemius, and H. H. G. Savenije (2008), The design of an optimal filter for monthly GRACE gravity models, *Geophys. J. Int.*, *175*, 417–432, doi:10.1111/j.1365-246X.2008.03922.x.

Klinker, E., F. Rabier, G. Kelly, and J.-F. Mahfouf (2000), The ECMWF operational implementation of four-dimensional variational assimilation. III: Experimental results and diagnostics with operational configuration, *Q. J. R. Meteorol. Soc.*, *126*, 1191–1215.

Kurtenbach, E., T. Mayer-Gürr, and A. Eicker (2009), Deriving daily snapshots of the Earth's gravity field from GRACE L1B data using Kalman filtering, *Geophys. Res. Lett.*, *36*, L17102, doi:10.1029/2009GL039564.

Kusche, J. (2007), Approximate decorrelation and non-isotropic smoothing of time-variable GRACE-type gravity field models, *J. Geod.*, *81*, 733–749, doi:10.1007/s00190-007-0143-3.

Loomis, B. (2009), Simulation study of a follow-on gravity mission to GRACE, Ph.D. dissertation, Colo. Cent. for Astrodyn. Res., Univ. of Colo. at Boulder, Boulder.

Luthcke, S. B., H. J. Zwally, W. Abdalati, D. D. Rowlands, R. D. Ray, R. S. Nerem, F. G. Lemoine, J. J. McCarthy, and D. S. Chinn (2006), Recent Greenland ice mass loss by drainage system from satellite gravity observations, *Science*, *314*, 1286–1289, doi:10.1126/science.1130776.

Lyard, F., F. Lefèvre, T. Letellier, and O. Francis (2006), Modelling the global ocean tides: Modern insights from FES2004, *Ocean Dyn.*, *56*, 394–415, doi:10.1007/s10236-006-0086-x.

Marchetti, P., J. J. Blandino, and M. A. Demetriou (2008), Electric propulsion and controller design for drag-free spacecraft operation, *J. Spacecraft Rockets*, *44*(6), 1303–1315, doi:10.2514/1.36307.

Messiah, A. (1962), Clebsch-Gordon (C.-G.) coefficients and '3 j' symbols, in *Quantum Mechanics*, vol. 2, pp. 1054–1060, North-Holland, Amsterdam.

Mueller, G., I. Thorpe, P. McNamara, and J. Camp (2005), Laser frequency stabilization for LISA, *NASA Tech. Memo. 2005-212794*, 24 pp.

Panet, I., V. Mikhailov, M. Diament, F. Pollitz, G. King, O. de Viron, M. Holschneider, R. Biancale, and J. M. Lemoine (2007), Coseismic and post-seismic signatures of the Sumatra 2004 December and 2005 March earthquakes in GRACE satellite gravity, *Geophys. J. Int.*, *171*, 177–190, doi:10.1111/j.1365-246X.2007.03525.x.

Pavlis, D. E., C. Deng, and J. J. McCarthy (2010), GEODYN Operations Manual, *Contract. Rep.*, SGT Inc., Greenbelt, Md.

Pierce, R., J. Leitch, M. Stephens, P. Bender, and R. Nerem (2008), Intersatellite range monitoring using optical interferometry, *Appl. Optics*, *47*(27), 5007–5019, doi:10.1364/AO.47.005007.

Ray, R. D. (1999), A global ocean tide model from TOPX/POSEIDON altimetry: GOT99.2, *NASA Tech. Memo. 209478*, 58 pp.

Reubelt, T., N. Sneeuw, and M. A. Sharifi (2009), Future mission design options for spatiotemporal geopotential recovery, paper presented at GGEO (Gravity, Geoid, and Earth Observation) Symposium, Chania, Crete, Greece, 23–27 June.

Rodell, M., et al. (2004), The global land data assimilation system, *Bull. Am. Meteorol. Soc.*, *85*, 381–394.

Rowlands, D. D., R. D. Ray, D. S. Chinn, and F. G. Lemoine (2002), Short-arc analysis of intersatellite tracking data in a gravity mapping mission, *J. Geod.*, *76*, 307–316, doi:10.1007/s00190-002-0255-8.

Save, H. V. (2009), Using regularization for error reduction in GRACE gravity estimation, Ph.D. dissertation, Cent. for Space Res., Univ. of Tex. at Austin, Austin.

Schrama, E. J. O., B. Wouters, and D. A. Lavallée (2007), Signal and noise in gravity recovery and climate experiment (GRACE) observed surface mass variations, *J. Geophys. Res.*, *112*, B08407, doi:10.1029/2006JB004882.

Simons, F. J., F. A. Dahlen, and M. A. Wieczorek (2006), Spatiospectral concentration on a sphere, *SIAM Rev.*, *48*(3), 504–536, doi:10.1137/S0036144504445765.

St. Rock, B., J. J. Blandino, and M. A. Demetriou (2006), Propulsion requirements for drag-free operation of spacecraft in low Earth orbit, *J. Spacecraft Rockets*, *43*(3), 594–606, doi:10.2514/1.15819.

Swenson, S., and J. Wahr (2002), Methods for inferring regional surface-mass anomalies from Gravity Recovery and Climate Experiment (GRACE) measurements of time-variable gravity, *J. Geophys. Res.*, *107*(B9), 2193, doi:10.1029/2001JB000576.

Swenson, S., and J. Wahr (2006), Post-processing removal of correlated errors in GRACE data, *Geophys. Res. Lett.*, *33*, L08402, doi:10.1029/2005GL025285.

Tapley, B. D., S. Bettadpur, M. Watkins, and C. Reigber (2004), The gravity recovery and climate experiment: Mission overview and early results, *Geophys. Res. Lett.*, *23*, L09607, doi:10.1029/2004GL019920.

Thompson, P. F., S. V. Bettadpur, and B. D. Tapley (2004), Impact of short period, non-tidal, temporal mass variability on GRACE gravity estimates, *Geophys. Res. Lett.*, *31*, L06619, doi:10.1029/2003GL019285.

Ullman, R. (1997), SOLVE program mathematical formulation, *Rep. HSTX- G and G-9201*, Raytheon ITSS, Greenbelt, Md.

van Dam, T., P. Visser, N. Sneeuw, M. Losch, T. Gruber, J. Bamber, M. Bierkens, M. King, and M. Smit (2008), Monitoring and modelling individual sources of mass distribution and transport in the Earth system by means of satellites, *Contract 20403*, Eur. Space Agency, Paris.

Visser, P. N. A. M., N. Sneeuw, T. Reubelt, M. Losch, and T. van Dam (2010), Space-borne gravimetric satellite constellations and ocean tides: aliasing effects, *Geophys. J. Int.*, *181*, 789–805, doi:10.1111/j.1365-246X.2010.04557.x.

Wahr, J., M. Molenaar, and F. Bryan (1998), Time variability of the Earth's gravity field: Hydrological and oceanic effects and their possible detection using GRACE, *J. Geophys. Res.*, *103*, 30,205–30,229.

Wieczorek, M. A., and F. J. Simons (2005), Localized spectral analysis on the sphere, *Geophys. J. Int.*, *162*, 655–675, doi:10.1111/j.1365-246X.2005.02687.x.

Wiese, D. N. (2011), Optimizing two pairs of GRACE-like satellites for recovering temporal gravity variations, Ph.D. dissertation, Colo. Cent. for Astrodyn. Res., Univ. of Colo. at Boulder, Boulder.

Wiese, D. N., W. M. Folkner, and R. S. Nerem (2009), Alternative mission architectures for a gravity recovery satellite mission, *J. Geod.*, *83*, 569–581, doi:10.1007/s00190-008-0274-1.

Wiese, D. N., R. S. Nerem, and F. G. Lemoine (2011a), Design considerations for a dedicated gravity recovery satellite mission consisting of two pairs of satellites, *J. Geod.*, doi:10.1007/s00190-011-0493-8, in press.

Wiese, D. N., P. N. A. M. Visser, and R. S. Nerem (2011b), Estimating low resolution gravity fields at short time intervals to reduce temporal aliasing errors, *Adv. Space Res.*, *48*, 1094–1107, doi:10.1016/j.asr.2011.05.027.

Wouters, B., and E. J. O. Schrama (2007), Improved accuracy of GRACE gravity solutions through empirical orthogonal function filtering of spherical harmonics, *Geophys. Res. Lett.*, *34*, L23711, doi:10.1029/2007GL032098.

S.-C. Han, Planetary Geodynamics Laboratory, Code 698, NASA Goddard Space Flight Center, Greenbelt, MD 20771, USA. (shin-chan.han@nasa.gov)

R. S. Nerem and D. N. Wiese, Colorado Center for Astrodynamics Research, Aerospace Engineering Sciences Department, University of Colorado at Boulder, 431 UCB, Boulder, CO 803039, USA. (wiese@colorado.edu; nerem@colorado.edu)